



# Measurements of the Zeeman effect in the $A^2\Pi$ and $B^2\Sigma^+$ states of calcium fluoride



J. Devlin<sup>a</sup>, M.R. Tarbutt<sup>a</sup>, D.L. Kokkin<sup>b</sup>, T.C. Steimle<sup>b,\*</sup>

<sup>a</sup> Centre for Cold Matter, Blackett Laboratory, Imperial College London, London SW7 2BW, United Kingdom

<sup>b</sup> Department of Chemistry and Biochemistry, Arizona State University, Tempe, AZ 85287-1604, United States

## ARTICLE INFO

### Article history:

Received 9 July 2015

In revised form 26 July 2015

Available online 30 July 2015

### Keywords:

Calcium fluoride  
Optical Zeeman  
g-factors

## ABSTRACT

The magnetic tuning of the low rotational levels in the  $(\nu=0)$   $X^2\Sigma^+$ ,  $(\nu=0)$   $A^2\Pi$ , and  $(\nu=0)$   $B^2\Sigma^+$  electronic states of calcium monofluoride, CaF, have been experimentally investigated using high resolution optical Zeeman spectroscopy of a cold molecular beam. The observed Zeeman shifts and splittings are successfully modeled using a traditional effective Hamiltonian approach to account for the interaction between the  $(\nu=0)$   $A^2\Pi$  and  $(\nu=0)$   $B^2\Sigma^+$  states. The determined magnetic  $g$ -factors for the  $X^2\Sigma^+$ ,  $B^2\Sigma^+$  and  $A^2\Pi$  states are compared to those predicted by perturbation theory.

© 2015 Elsevier Inc. All rights reserved.

## 1. Introduction

The successful magneto-optical trapping (MOT) of SrF molecules [1,2] has invoked interest in similar molecules such as CaF [3]. In the case of SrF the  $A^2\Pi_{1/2}-X^2\Sigma^+$  transition was employed as the laser cooling transition. The mechanism of magneto-optical trapping for SrF and related molecules, has been elucidated in Ref. [4] where a rate model was used to model the interaction of the molecules with multiple frequencies of laser light. It was shown that the correct choice of laser polarization depends upon the sign of the upper state magnetic  $g$ -factor,  $g_u$ , and that there is no trapping force if  $g_u$  is zero. In cases where  $g_u$  is much smaller than the lower state  $g$ -factor,  $g_l$ , the trapping forces are weak. In the Hund's case (a) limit a  $^2\Pi_{1/2}$  state has a negligibly small  $g$ -factor and so is unsuitable for making a MOT. The observed MOT of SrF was attributed to the mixing of the  $(\nu=0)$   $A^2\Pi_{1/2}$  state with the  $(\nu=0)$   $B^2\Sigma^+$  state, resulting in a value of  $g_u$ , that is large enough for weak trapping. For CaF, the value of  $g_u$  for the  $A^2\Pi_r$  state is predicted to be smaller than for SrF, and it is unclear whether a MOT is feasible using this transition. An alternative is to use the  $B^2\Sigma^+-X^2\Sigma^+$  transition so that  $g_u$  and  $g_l$  are comparable. These considerations highlight the importance of knowing accurately the  $g$ -factors of the  $A^2\Pi_r$  and  $B^2\Sigma^+$  states of CaF. Here we precisely experimentally determine the magnetic  $g$ -factors for the  $(\nu=0)$   $A^2\Pi_{1/2}$ ,  $(\nu=0)$   $A^2\Pi_{3/2}$ , and  $(\nu=0)$   $B^2\Sigma^+$  states of CaF from the analysis of the optical Zeeman spectra of a cold molecule beam.

A model of the Zeeman effect in diatomic molecules was first developed by Hill [5] and dates back to the early days of quantum mechanics. In that model, the Zeeman operator was taken simply as:

$$\hat{H}^{\text{Ze}} = \mu_B B_Z (g_L \hat{L}_Z + g_S \hat{S}_Z), \quad (1)$$

where  $B_Z$ ,  $\hat{L}_Z$ , and  $\hat{S}_Z$  are the space-fixed components of the magnetic field, electronic orbital angular momentum and electronic spin angular momentum operators, respectively. The magnetic  $g$ -factors,  $g_L$  and  $g_S$ , were taken as 1.0 and 2.0, respectively. Analysis of the magnetic field effect of the  $(0,0)$   $B^2\Sigma^+-X^2\Sigma^+$  band of CaH by Watson in 1932 [6] showed that the observations could only be reproduced by adding to Hill's model a phenomenological, rotationally dependent term. The form of the correction term was based upon speculation that the departure from Hill's model was due to the mixing of the  $(\nu=0)$   $B^2\Sigma^+$  state with levels of the  $A^2\Pi$  state, analogous to the source of the spin-rotation interaction which was already well understood. Thus, the importance of non-adiabatic contributions to describing the Zeeman effect, which is the focus of the current study, was realized 80 years ago.

Modern analyses of the Zeeman effect in diatomic molecules typically are based upon an effective Hamiltonian model. The Zeeman operator has off-diagonal matrix elements connecting not only different rotational states, but also different vibrational and electronic states. The effects of these terms are treated by replacing the total Hamiltonian with an effective Hamiltonian that operates only in the rotational subspace of a single vibronic state. The molecular parameters which define the effective Hamiltonian treat the non-adiabatic effects. The physical meaning of these

\* Corresponding author.

parameters is garnered by a comparison with the expressions derived from a second order perturbation treatment of the total Hamiltonian. Ignoring the small magnetic moments associated with rotational and nuclear spin contributions, the effective Zeeman Hamiltonian is [7,8]:

$$\begin{aligned} \hat{H}_{\text{eff}}^{\text{Zee}} = & g_S \mu_B \hat{\mathbf{S}} \cdot \hat{\mathbf{B}} + g'_L \mu_B \hat{\mathbf{L}} \cdot \hat{\mathbf{B}} + g_L \mu_B (\hat{S}_x \hat{B}_x + \hat{S}_y \hat{B}_y) \\ & + g'_L \mu_B (e^{-2i\phi} \hat{S}_+ \hat{B}_+ + e^{+2i\phi} \hat{S}_- \hat{B}_-) \end{aligned} \quad (2)$$

where  $\hat{S}_x$  and  $\hat{B}_x$  refer to the  $x$ -axis molecule-fixed components of the electronic spin angular momentum and magnetic field, respectively, and  $\phi$  is the azimuthal angle of the electronic coordinates. The electronic spin  $g$ -factor,  $g_S$ , and the orbital  $g$ -factor,  $g'_L$ , of the effective Hamiltonian are regarded as variables and can differ significantly from 2.002 and unity because of the non-adiabatic contributions. The value of the anisotropic  $g$ -factors,  $g_L$  and  $g'_L$ , are often difficult to predict *a priori* and also need to be considered as variables. The parity dependent term  $g'_L$  is only required for states with non-zero electronic orbital angular momentum. Modeling the Zeeman effect in a  $^2\Sigma^+$  state requires varying  $g_L$ , and to a lesser extent  $g_S$ , while modeling the Zeeman effect in a state with non-zero orbital angular momentum requires varying  $g'_L$ ,  $g_L$ ,  $g'_S$  and possibly  $g_S$ . In the case of an interacting  $^2\Sigma^+$  and  $^2\Pi$  pair of states, which is often the case, an estimate for  $g_L$  is obtainable from the Curl relationship [9]:

$$g_L \approx -\gamma/2B, \quad (3)$$

where  $\gamma$  and  $B$ , are the spin-rotation and rotational parameters respectively. Furthermore, the parity-dependent anisotropic  $g$ -factor,  $g'_L$ , of the  $^2\Pi$  state can be approximated using an equation analogous to the Curl relationship [7,8]:

$$g'_L \approx p/2B, \quad (4)$$

where  $p$  is the  $\Lambda$ -doubling parameter.

The effective Hamiltonian approach is only applicable when there are no local perturbations. The objective of the current study is to ascertain if the effective Hamiltonian approach is applicable, and if so, determine  $g'_L$ ,  $g_L$ ,  $g'_S$  and  $g_S$  for the  $(\nu=0)$   $A^2\Pi_{1/2}$ ,  $(\nu=0)$   $A^2\Pi_{3/2}$ ,  $(\nu=0)$   $B^2\Sigma^+$  and  $(\nu=0)$   $X^2\Sigma^+$  states of CaF. The appropriateness of the effective Hamiltonian approach for modeling the  $(\nu=0)$   $B^2\Sigma^+$  state is suspect given that the energy levels for this state are embedded in those of high vibrational levels of the  $A^2\Pi$  state. The analysis of the Zeeman effect requires a precise determination of the field-free energy levels. Hence, a secondary goal is to precisely model the field-free energies of the  $(\nu=0)$   $A^2\Pi_{1/2}$ ,  $(\nu=0)$   $A^2\Pi_{3/2}$ , and  $(\nu=0)$   $B^2\Sigma^+$  states that can be used to describe the tuning of all optical transitions in these band systems.

There have been no previous experimental studies of the magnetic tuning of the optical transitions of CaF, but there are numerous previous reports on the field-free spectroscopy of this molecule. The fine and magnetic hyperfine parameters for the  $(\nu=0)$   $X^2\Sigma^+$  state of CaF have been precisely determined from the analysis of the pure rotational spectrum [10]. The current most precisely determined field-free parameters for the  $A^2\Pi$  and  $B^2\Sigma^+$  states of CaF are found in Ref. [11], which describes the analysis of the laser excitation spectrum of the  $(0,0)$   $A^2\Pi-X^2\Sigma^+$  and  $(1,1)$   $A^2\Pi-X^2\Sigma^+$  systems measured with Doppler-limited resolution. The line positions were measured to an absolute precision of  $0.01 \text{ cm}^{-1}$  and the resolution was insufficient to resolve the  $^{19}\text{F}$  magnetic hyperfine interaction. The results were combined with the previously recorded Doppler-limited spectrum of the  $B^2\Sigma^+-X^2\Sigma^+$  transition [12] and a de-perturbation of the  $A^2\Pi$  and  $B^2\Sigma^+$  states performed. Vergès et al. [13] reported on the high resolution Fourier transform emission spectroscopy of CaF pumped by fixed frequency lines of a krypton-ion laser. Via a step-wise global

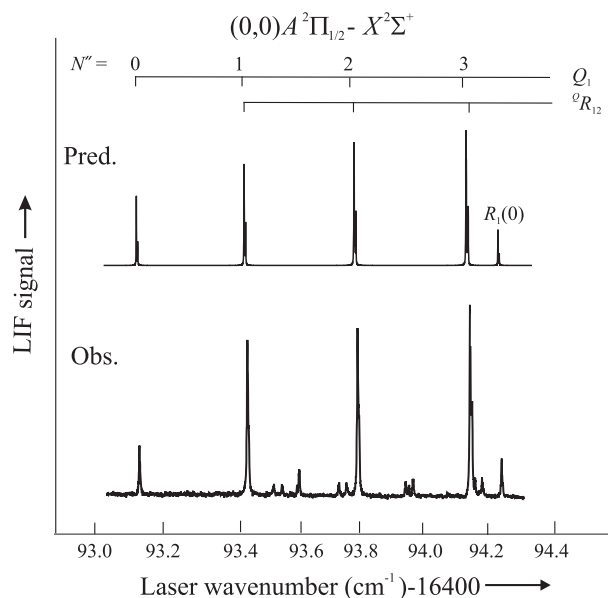


**Fig. 1.** The observed and predicted field-free spectrum in the regions of the low- $J$   $Q_1$  and  $Q_{12}$  branch features of  $A^2\Pi_{1/2}-X^2\Sigma^+$  band.

fit of all their observed lines they were able to reproduce the wavenumbers of more than 1200 lines of the  $X^2\Sigma^+$ ,  $A^2\Pi$ ,  $B^2\Sigma^+$ ,  $B^2\Delta$ ,  $D^2\Sigma^+$  and  $C^2\Pi$  states within experimental uncertainties ( $0.007 \text{ cm}^{-1}$ ).

## 2. Experiment

The Zeeman spectrometer, supersonic molecular beam production method, and laser induced fluorescence detection scheme are similar to that used in the study of CaH [14]. A variable speed rotating Ca metal rod was ablated in the presence of a (95%) Ar/(5%)  $\text{SF}_6$  gas mixture. The pulsed free jet expansion was skimmed to form a well collimated molecular beam which was crossed with a continuous wave, single longitudinal mode, dye laser approximately 20 cm from the source. A relatively high backing pressure of approximately 3 MPa was used to cool the molecules to a rotational temperature of less than 15 K. The laser power was attenuated to approximately 20 mW and lightly focused to avoid power broadening. Spectral line widths of less than 40 MHz full width at half maximum were obtainable by this combination of beam collimation and low laser power. The relative wavenumbers were measured by simultaneously recording the transmission through an actively stabilized, calibrated, confocal etalon. The absolute wavenumber calibration was obtained by simultaneously recording the sub-Doppler absorption spectrum of a heated gaseous  $\text{I}_2$  cell [15].

The Zeeman spectra were recorded using field strengths of 3163 and 5296 G, which were generated by rare earth magnets attached to an iron yoke. The molecular beam passed through 5.0 mm holes in the center of the magnet/yoke assembly. A polarization rotator was used to align the electric field vector of the linearly polarized laser radiation either perpendicular ( $\perp$ ) or parallel ( $\parallel$ ) to the static magnetic field vector. The magnetic field was measured with a commercial Hall probe Gauss meter and independently checked by recording and analyzing the Zeeman spectrum of the  $(4s4p)^3P_1-(4s5s)^3S_1$  transition of atomic calcium [16]. The combined systematic error associated with the measurement of the magnetic field induced frequency shifts and the field strength is estimated to be less than 1%.

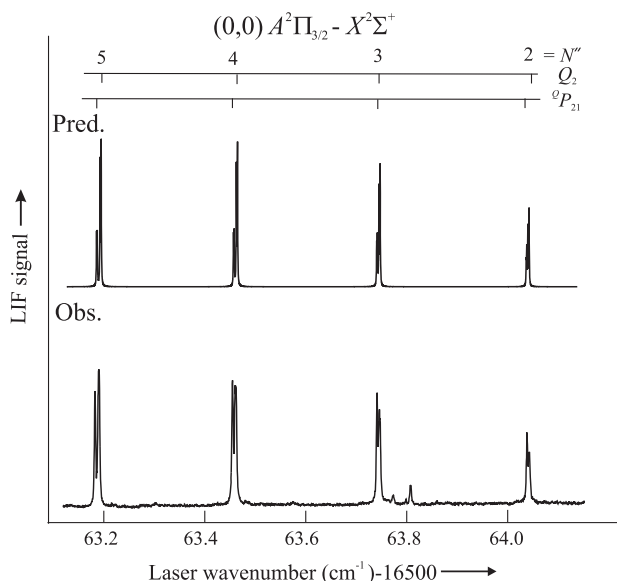


**Fig. 2.** The observed and predicted field-free spectrum in the regions of the low- $J$   $Q_2$  and  $Q_{21}$  branch features of the  $A^2\Pi_{3/2}-X^2\Sigma^+$  band.

### 3. Observation

The low- $J$  branch features of the  $(0,0)$   $A^2\Pi-X^2\Sigma^+$  and  $(0,0)$   $B^2\Sigma^+-X^2\Sigma^+$  bands were recorded field-free and analyzed because the precision of the present measurements are significantly higher than the previous measurements [11–13]. The field-free spectrum in the regions of the low- $J$   $Q_1$  and  $Q_{12}$  branch features of  $A^2\Pi_{1/2}-X^2\Sigma^+$  band and the  $Q_2$  and  $Q_{21}$  branch features of the  $A^2\Pi_{3/2}-X^2\Sigma^+$  band are given in Figs. 1 and 2, respectively. The conventional  $^2\Pi$  (case  $a_{\beta J}$ )– $^2\Sigma^+$  (case  $b_{\beta J}$ ) labeling scheme of  $\Delta N \Delta J_{F_i F_i''}(N'')$  is used. In this nomenclature the first subscript,  $F_i$ , has  $i=1$  for the  $A^2\Pi_{1/2}$  component and  $i=2$  for  $A^2\Pi_{3/2}$ , while the second subscript,  $F_i''$ , has  $i=1$  or  $2$  for  $J=N+1/2$  or  $N-1/2$ , respectively. When  $F_i = F_i''$  the second subscript is dropped. Also

presented in Figs. 1 and 2 are the predicted spectra obtained using the optimized parameters (see below). A 20 MHz full width at half maximum (FWHM) was used in the prediction, which is slightly less than the observed linewidth of 35 MHz, to reveal unresolved structure. Scans over the low- $J$  branch features exhibited splitting due to the  $^{19}\text{F}$  ( $I=1/2$ ) magnetic hyperfine interaction in the  $X^2\Sigma^+$  state. This is illustrated in Fig. 3 where the observed and predicted spectra in region of the  $R_1(1)$ ,  $R_2(1)$ ,  $Q_{21}(1)$  and  $^R S_{12}(1)$  features of the  $(0,0)$   $B^2\Sigma^+-X^2\Sigma^+$  band are presented. The energy level pattern and associated assignments are also given. The observed  $^R S_{12}(1)$  hyperfine-induced transition, feature “B” of Fig. 3, is relatively strong because the hyperfine interaction in the  $N=1$  level of the  $X^2\Sigma^+$  state is large relative to the spin–rotation splitting (i.e.  $J$  is not a good quantum number). Although the relative intensities of the predicted spectra for the  $(0,0)$   $A^2\Pi_{1/2}-X^2\Sigma^+$  and  $(0,0)$   $B^2\Sigma^+-X^2\Sigma^+$  bands given in Figs. 1 and 3 are in good agreement with the observed spectra, the intensities of the predicted spectrum for the first members ( $N''=2$  and  $3$ ) of the  $Q_2$  and  $Q_{21}$  branches of the  $(0,0)$   $A^2\Pi_{3/2}-X^2\Sigma^+$  band (Fig. 2) differ from the observation. Specifically, the satellite  $Q_{21}$  line, which is at the lower wavenumber side, is observed to be more intense than the main  $Q_2$  line, which appears at the high wavenumber side. This apparent discrepancy is attributed to saturation of the transition due to the relatively high laser power used and variation in molecular production. The relative intensities of the observed spectra for the other four branches of the  $(0,0)$   $A^2\Pi_{3/2}-X^2\Sigma^+$  band (not shown) are in closer agreement with prediction. The observed transition wavenumbers, quantum number assignments and the residuals from the subsequent analysis (see below) for the  $(0,0)$   $A^2\Pi-X^2\Sigma^+$  and  $(0,0)$   $B^2\Sigma^+-X^2\Sigma^+$  bands are presented in Tables 1 and 2, respectively.

The region between  $16563.6\text{ cm}^{-1}$  and  $16565.9\text{ cm}^{-1}$  of the  $(0,0)$   $A^2\Pi_{3/2}-X^2\Sigma^+$  band,  $16490.9\text{ cm}^{-1}$  and  $16494.3\text{ cm}^{-1}$  of the  $(0,0)$   $A^2\Pi_{1/2}-X^2\Sigma^+$  band, and  $18831.7\text{ cm}^{-1}$  and  $18834.9\text{ cm}^{-1}$  of the  $(0,0)$   $B^2\Sigma^+-X^2\Sigma^+$  band were recorded in the presence of a static magnetic field. The observed spectrum in the region of the low- $J$   $Q_{12}$  and  $P_1$  branch features of the  $(0,0)$   $A^2\Pi_{1/2}-X^2\Sigma^+$  band recorded in the presence of a 5296 G magnetic field oriented parallel ( $\Delta M_J=0$ ) to the electric field of the laser radiation is presented in

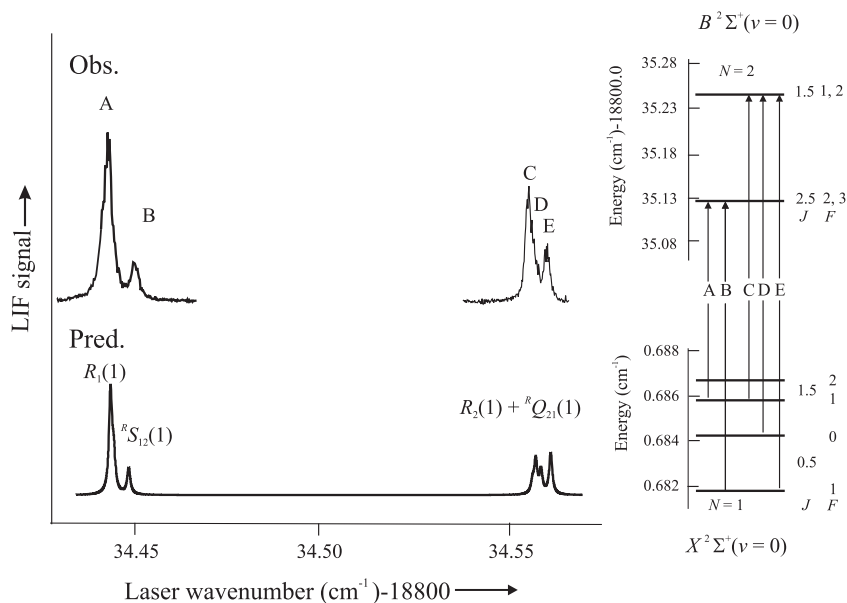


**Fig. 3.** The observed and predicted field-free spectrum in the regions of the  $R_1(1)$ ,  $R_2(1)$ ,  $Q_{21}(1)$  and  $^R S_{12}(1)$  features of the  $(0,0)$   $B^2\Sigma^+-X^2\Sigma^+$  band and the associated energy levels. The  $^R S_{12}(1)$  transition is relatively intense because the magnetic hyperfine splitting is comparable to the spin–rotation splitting in the  $N=1$  rotational level of the  $X^2\Sigma^+$  state.

**Table 1**The observed and calculated transition wavenumbers ( $\text{cm}^{-1}$ ) for the (0,0)  $A^2\Pi-X^2\Sigma^+$  band system of CaF.

Branch <sup>a</sup>	$J''$	$F''$	$F'$	Obs. <sup>b</sup>	Obs. – calc.	Branch	$J''$	$F''$	$F'$	Obs.	Obs. – calc
$P_2(3)$	2.5	2	1	562.0026	0.0005	$Q_1(0)$	0.5	1	0	493.1163	–0.0006
		3	2	562.0050	0.0005	$Q_1(1)$	1.5	2.1	2.1	493.4463	0.0002, –0.0007
$^pO_{21}(3)$	3.5	3	2	562.0001	0.0014	$Q_1(2)$	2.5	3.2	3.2	493.7825	0.0006, –0.0005
$^qP_{21}(2)$	2.5	3.2	2.1	564.0526	–0.0004, –0.0015	$Q_1(3)$	3.5	4.3	4.3	494.1249	0.0006, –0.0007
$^qP_{21}(3)$	3.5	4.3	3.2	563.7436	0.0012, –0.0001	$Q_1(4)$	4.5	5.4	5.4	494.4742	0.0008, –0.0006
$^qP_{21}(4)$	4.5	5.4	4.3	563.4460	0.0010, –0.0004	$Q_1(5)$	5.5	6.5	6.5	494.8307	0.0016, 0.0002
$^qP_{21}(5)$	5.5	6.5	5.4	563.1612	0.0006, –0.0009	$^qR_{12}(1)$	0.5	1	2	493.4503	–0.0007
$^qP_{21}(6)$	6.5	7.6	6.5	562.8894	0.0001, –0.0015	$^qR_{12}(2)$	1.5	2	3	493.7870	–0.0008
$^qP_{21}(7)$	7.5	8.7	7.6	562.6336	0.0025, 0.0009	$^qR_{12}(3)$	2.5	2	3	494.1287	–0.0003
$Q_2(2)$	1.5	1	1	564.0560	–0.0004		3	4	4	494.1311	–0.0003
		2	2	564.0581	–0.0008	$^qR_{12}(4)$	3.5	3	4	494.4781	–0.0012
$Q_2(3)$	2.5	2.3	2.3	563.7489	0.0018, –0.0007		4	5	5	494.4812	–0.0004
$Q_2(4)$	3.5	3.4	3.4	563.4525	0.0015, –0.0008	$^qR_{12}(5)$	4.5	4.5	5.6	494.8372	0.0009, –0.0014
$Q_2(5)$	4.5	4.5	4.5	563.1692	0.0013, –0.0009	$R_1(0)$	0.5	1	2	494.2219	–0.0002
$Q_2(6)$	5.5	5.6	5.6	562.8994	0.0015, –0.0007		0	1		494.2256	–0.0006
$Q_2(7)$	6.5	6	6	562.6404	–0.0007	$R_1(2)$	2.5	2	3	496.3607	–0.0008
		7	7	562.6441	0.0009		2	3		496.3652	–0.0012
$^sR_{21}(0)$	0.5	1	2	566.1091	0.0000	$P_1(1)$	1.5	2.1	1.0	492.4777	0.0012, 0.0003
		0	1	566.1128	–0.0004	$P_1(2)$	2.5	3.2	2.1	492.1656	–0.0003, –0.0014
$^sR_{21}(1)$	1.5	2.1	3.2	567.1696	0.0010, 0.0002	$P_1(3)$	3.5	4.3	3.2	491.8681	0.0015, –0.0009
		1	2	567.1736	0.0001	$P_1(4)$	4.5	5	4	491.5718	0.0014
$^sR_{21}(2)$	2.5	3.2	4.3	568.2421	0.0011, 0.0000		4	3	3	491.5737	0.001
		2	3	568.2470	0.0000	$P_1(6)$	6.5	7.6	6.5	490.9896	0.0003, –0.0012
$^RQ_{21}(1)$	1.5	2.1	2.1	565.4235	0.0000, –0.0009	$^pQ_{12}(1)$	0.5	0	1	492.4777	–0.0011
$^RQ_{21}(2)$	2.5	3.2	3.2	565.7987	0.0008, –0.0003		1	1		492.4816	0.0002
$^RQ_{21}(3)$	3.5	4.3	4.3	566.1851	–0.0001, –0.0014	$^pQ_{12}(2)$	1.5	1.2	1.2	492.1709	0.0016, –0.0010
$^RQ_{21}(4)$	5.5	5.4	5.4	566.5857	0.0002, –0.0012	$^pQ_{12}(3)$	2.5	2.3	2.3	491.8626	0.0007, –0.0006
$^RQ_{21}(5)$	5.5	6.5	6.5	566.9989	0.0003, –0.0012	$^pQ_{12}(4)$	3.5	3.4	3.4	491.5661	0.0017, 0.0002
$^RQ_{21}(6)$	6.5	7.6	7.6	567.4245	–0.0002, –0.0018	$^pQ_{12}(6)$	5.5	5.6	5.6	490.9988	0.0009, –0.0013
$R_2(1)$	0.5	1	1	565.4280	–0.0005	$^oP_{12}(2)$	1.5	1	0	491.0622	–0.0020
$R_2(2)$	1.5	1	2	565.8010	–0.0003		2	1		491.0663	–0.0004
		2	3	565.8033	–0.0006	$^oP_{12}(3)$	2.5	3	2	490.0229	0.0016
$R_2(3)$	2.5	2	3	566.1893	–0.0006		2	1		490.0264	0.0017
		3	4	566.1918	–0.0005		3	2		490.0287	0.0017
$R_2(4)$	3.5	3	4	566.5901	–0.0013						
		4	5	566.5959	0.0021						
$R_2(5)$	4.5	4.5	5.6	567.0078	0.0019, –0.0004						
$R_2(6)$	5.5	5.6	6.7	567.4335	0.0002, –0.0020						

<sup>a</sup> A  $^{\Delta N} \Delta J_{F'F''}(N'')$  branch designation is used. In cases where there are two entries for a single observed transition wavenumber the hyperfine splitting in the  $X^2\Sigma^+$  state is not resolved.

<sup>b</sup> The transition wavenumber  $-16000 \text{ cm}^{-1}$ .

Fig. 4. Also presented are the predicted spectra for magnetic fields ranging from 0 G to 5300 G. The large magnetic-field-induced spectral shifts of the (0,0)  $A^2\Pi_{1/2}-X^2\Sigma^+$  band features are due to the rapid tuning of the  $X^2\Sigma^+$  state levels. The levels of the  $A^2\Pi_{1/2}$  state magnetically tune much more slowly as is illustrated in Fig. 5 where the tuning of the energy levels associated with the  $P_1(3)$  and  $^pQ_{12}(3)$  lines are presented. The  $P_1$ ,  $^pQ_{12}$ , and  $R_1$  branch features of the (0,0)  $A^2\Pi_{1/2}-X^2\Sigma^+$  band are associated with the upper energy,  $e$ -parity (+) component of the  $\Lambda$ -doublet, which exhibit a very weak magnetic tuning causing only a broadening and partial splitting of the observed spectrum in Fig. 4. The  $^oR_{12}$ ,  $Q_1$ , and  $^oP_{12}$  branch features of the (0,0)  $A^2\Pi_{1/2}-X^2\Sigma^+$  band are associated with the lower energy,  $f$ -parity (–) parity component of the  $\Lambda$ -doublet and exhibit a more significant splitting. In the effective Hamiltonian model, this parity dependent difference is due to  $g_I$ . As seen in Fig. 5, the electronic spin and nuclear spin projection quantum number,  $M_S (= \pm 1/2)$  and  $M_I (= \pm 1/2)$ , become approximately good upon application of only a modest magnetic field for the  $N = 3$  rotational level of the ( $v = 0$ )  $X^2\Sigma^+$  state because the electronic and nuclear spins are easily de-coupled from the molecular

axis. The hyperfine interaction is negligible in the  $A^2\Pi$  state and  $J$  is the appropriate total angular momentum quantum number in the absence of the magnetic field. The electron spin is strongly coupled to the molecular axis in the  $A^2\Pi$  state via spin–orbit coupling and the appropriate projection quantum number is  $M_J$  for the field strengths used.

The observed spectrum in the region of the low- $J$   $^RQ_{21}$  and  $R_2$  branch features of the (0,0)  $A^2\Pi_{3/2}-X^2\Sigma^+$  band recorded in the presence of a 3163 G magnetic field oriented perpendicular ( $\Delta M_J = \pm 1$ ) to the electric field of the laser radiation is presented in Fig. 6. Also presented are the predicted spectra for magnetic fields ranging from 0 G to 3163 G. The magnetic tuning is rapid for both the  $A^2\Pi_{3/2}$  and  $X^2\Sigma^+$  levels associated with the transitions of Fig. 6 as is illustrated in Fig. 7 where the tuning of the energy levels associated with the  $^RQ_{21}(1)$  and  $R_2(1)$  lines are presented. The  $\Lambda$ -doubling in the  $J = 3/2$  level of the  $A^2\Pi_{3/2}$  state is negligible and the levels are a very near degenerate set with opposite parity. There is a slight non-linearity in the magnetic tuning due to interaction with the  $J = 5/2$  levels. In the Hund's case (a) limit the splitting at 3163 G between the  $M_J = 3/2$  and  $-3/2$  levels would be

**Table 2**The observed and calculated transition wavenumbers ( $\text{cm}^{-1}$ ) for the (0,0)  $B^2\Sigma^+-X^2\Sigma^+$  system of CaF.

Branch <sup>a</sup>	$J^2$	$F^2$	$F'$	Obs. <sup>b</sup>	Obs. – calc.	Branch <sup>a</sup>	$J^2$	$F^2$	$F'$	Obs. <sup>b</sup>	Obs. – calc.
$R_1(0)$	0.5	1	2	33.7864	0.0004	$P_{Q_{12}}(1)$	0.5	1	0	32.4450	–0.0008
		0	1	33.7900	–0.0001	$P_{Q_{12}}(2)$	1.5	2	1	31.7368	0.001
$R_1(1)$	1.5	2.1	3.2	34.4423	–0.0001, –0.0010		1	1	1	31.7339	0.0007
$R_{S_{12}}(1)$	0.5	1	2	34.4469	–0.0005	$P_{Q_{12}}(3)$	2.5	3	2	31.0244	0.001
$R_1(2)$	2.5	3.2	4.3	35.0971	0.0007, –0.0004		2	2	2	31.0219	0.0009
$R_{S_{12}}(2)$	1.5	2	3	35.1026	0.0002	$P_{Q_{12}}(4)$	3.5	4	3	30.3077	–0.001
$R_1(3)$	3.5	4.3	5.4	35.7483	0.0004, –0.0009	$P_{Q_{12}}(5)$	4.5	4	5	29.5910	–0.0008
$R_{S_{12}}(3)$	2.5	3	4	35.7549	–0.0001						
$R_1(4)$	4.5	5.4	6.5	36.3975	0.0004, –0.001	$P_1(1)$	1.5	2.1	1.0	32.4413	0.0004, –0.0005
$R_{S_{12}}(4)$	3.5	4	5	36.4063	0.0009	$P_1(2)$	2.5	3.2	2.1	31.7311	0.0013, 0.0001
						$P_1(3)$	3.5	4.3	3.2	31.0169	0.0006, –0.0007
$R_2(1)$	0.5	1	2	34.5613	–0.0011	$P_1(4)$	4.5	4.3	5.4	30.3002	–0.0002, –0.0016
		0	1	34.5591	–0.0006	$P_1(5)$	5.5	5.4	6.5	29.5839	0.0017, 0.0002
$R_2(2)$	1.5	2	3	35.2646	0.0012						
		1	2	35.2613	0.0005	$P_2(2)$	1.5	2	1	31.8046	–0.0002
$R_2(3)$	2.5	2	3	35.9589	–0.0007		1	0	0	31.8021	–0.0001
		3	4	35.9614	–0.0006	$P_2(3)$	2.5	3	2	31.1380	–0.0004
$R_2(4)$	3.5	3.4	4.5	36.6574	0.0013, –0.0010		2	1	1	31.1355	–0.0005
						$P_2(4)$	3.5	4	3	30.4636	0.0008
$R_{Q_{21}}(0)$	0.5	1	1	33.8550	0.0000		3	2	2	30.4687	0.0012
		0	1	33.8591	0.0000	$P_2(5)$	4.5	5	4	29.7909	0.0002
$R_{Q_{21}}(1)$	1.5	2.1	2.1	34.5569	–0.0005, –0.0014		4	3	3	29.7984	0.0019
$R_{Q_{21}}(2)$	2.5	3.2	3.2	35.2583	0.0009, –0.0002						
$R_{Q_{21}}(3)$	2.5	4	4	35.9540	–0.0009	$P_{O_{21}}(3)$	2.5	2	1	31.7998	–0.0001
		3.3	3.4	35.9561	–0.0002, –0.0002	$P_{O_{21}}(4)$	3.5	3	2	31.1328	0.0002
$R_{Q_{21}}(4)$	3.5	4	5	36.6506	–0.0009	$P_{O_{21}}(5)$	4.5	4	3	30.4705	0.0008
						$P_{O_{21}}(6)$	5.5	5	4	29.7984	–0.0003

Std. dev. =  $0.00081 \text{ cm}^{-1}$ 

<sup>a</sup> A  $\Delta N \Delta J F_1 F_1'$  branch designation is used. In cases where there are two entries for a single observed transition wavenumber the hyperfine splitting in the  $X^2\Sigma^+$  state is not resolved.

<sup>b</sup> The transition wavenumber  $-18800 \text{ cm}^{-1}$ .

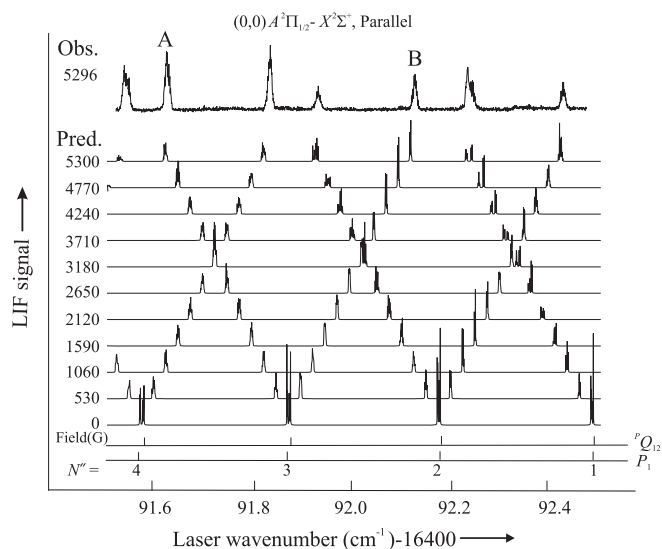


**Fig. 4.** The observed (top) and predicted (bottom) spectra in the region of the low- $J$   $P_{Q_{12}}$  and  $P_1$  branch features of the (0,0)  $A^2\Pi_{1/2}-X^2\Sigma^+$  band recorded in the presence of magnetic field oriented parallel ( $\Delta M_J = \pm 0$ ) to the electric field of the laser radiation. The energy levels associated with the “A” and “B” spectral features are given in Fig. 5. The predicted spectra were obtained using the optimized spectroscopic parameters. The  $N''$  assignments at zero field are given at the bottom of the graph.

10631 MHz as compared to the observed 10507 MHz. The predicted splitting at 3163 G in the  $X^2\Sigma^+$  state of 8955 MHz is very near the 8863 MHz value expected for a free electron.

The observed spectrum in the region of the low- $J$   $P_{Q_{12}}$ ,  $P_1$ , and  $P_2$  branch features of the (0,0)  $B^2\Sigma^+-X^2\Sigma^+$  band recorded in the presence of a 3163 G magnetic field oriented parallel ( $\Delta M_J = 0$ ) to the electric field of the laser radiation is presented in Fig. 8. Also

presented are the predicted spectra for magnetic fields ranging from 0 G to 3163 G. The magnetic tuning is rapid for both the  $B^2\Sigma^+$  and  $X^2\Sigma^+$  levels associated with the transitions of Fig. 8 as is illustrated in Fig. 9 where the tuning of the energy levels associated with the  $P_{Q_{12}}(2)$  and  $P_1(2)$  are presented. In large fields the  $B^2\Sigma^+$  and  $X^2\Sigma^+$  levels shift approximately parallel to one another, and so there is very little shift of the  $\Delta M_J = 0$  spectral lines with increasing magnetic field, as can be seen in Fig. 8. In the  $B^2\Sigma^+$  state  $M_J$  is the approximately good quantum number at low fields. The electron spin decouples from the rotation upon application of a modest field and the approximately good quantum numbers at high field are  $M_S$  and  $M_N$ . In the  $X^2\Sigma^+$  state this decoupling occurs at a much lower value of magnetic field because the spin-rotation interaction is 35 times smaller than in the  $B^2\Sigma^+$  state.

The observed transition wavenumbers, quantum number assignments and the residuals from the subsequent analysis (see below) for the (0,0)  $A^2\Pi-X^2\Sigma^+$  and (0,0)  $B^2\Sigma^+-X^2\Sigma^+$  bands are presented in Supplemental Tables 1 and 2, respectively. For the (0,0)  $A^2\Pi-X^2\Sigma^+$  band the data included 132 measured transition wavenumbers that were assigned to 309 transitions. For the (0,0)  $B^2\Sigma^+-X^2\Sigma^+$  band the data included 144 measured transition wavenumbers that were assigned to 266 transitions.

#### 4. Analysis

The fine and proton magnetic hyperfine structure for the observed low- $J$  transitions of the (0,0)  $A^2\Pi-X^2\Sigma^+$  and (0,0)  $B^2\Sigma^+-X^2\Sigma^+$  bands systems were modeled with a traditional effective Hamiltonian operator [7] approach. This differs from the “deperturbation” approach used in the previous analysis [11], where the energies were predicted by explicitly including the spin-orbit and rotational mixing terms between the  $A^2\Pi$  and  $B^2\Sigma^+$  states. In the effective Hamiltonian approach the effects of rotational and spin-orbit induced mixing of the various



**Table 3**

The determined field-free spectroscopic parameters for the (0,0)  $A^2\Pi-X^2\Sigma^+$  and (0,0)  $B^2\Sigma^+-X^2\Sigma^+$  band system transition wavenumbers of CaF (Tables 1 and 2).

Parameter <sup>a</sup>	$A^2\Pi$ ( $\nu=0$ )		Parameter	$B^2\Sigma^+$ ( $\nu=0$ )	
	This work <sup>b,c</sup>	Previous <sup>d</sup>		This work <sup>b,c</sup>	Previous <sup>d</sup>
$A$	72.61743 (47)	72.589 (2)	$B$	0.341259 (17)	0.341279 (17)
$B$	0.347395 (11)	0.347527 (16)	$\gamma$	−0.045994 (90)	−0.045770 (77)
$A_D$	−0.000149 (23)	0.0000192 (10)	$T_0$ ( $B^2\Sigma^+$ )	18833.12751 (26)	18833.152 (2)
$p+2q$	−0.0452 (12)	−0.045109 (48)			
$q$	−0.0002916 (fixed)	−0.0002916 (16)			
$T_0$ ( $A^2\Pi$ )	16529.10177 (24)	16529.134 (1)			

<sup>a</sup> All units in wavenumbers ( $\text{cm}^{-1}$ ).

<sup>b</sup> Numbers in parentheses represent a 2 $\Sigma$  error estimate in the last quoted decimal point. For example the error in the spin-orbit parameter,  $A$ , is  $0.00047 \text{ cm}^{-1}$ . The centrifugal distortion constants,  $D$ , for the  $A^2\Pi$  ( $\nu=0$ ) and  $B^2\Sigma^+$  ( $\nu=0$ ) states were held fixed to the  $4.809 \times 10^{-7} \text{ cm}^{-1}$  [13] and  $4.833 \times 10^{-7} \text{ cm}^{-1}$  [13], respectively.

<sup>c</sup> The  $X^2\Sigma^+$  ( $\nu=0$ ) state parameters were held fixed to those of Ref. [10]:  $B = 0.34248822 \text{ cm}^{-1}$ ,  $D = 4.969 \times 10^{-7} \text{ cm}^{-1}$ ,  $\gamma = 1.3138 \times 10^{-3} \text{ cm}^{-1}$ ,  $b_F = 0.004089 \text{ cm}^{-1}$ , and  $c = 0.00111 \text{ cm}^{-1}$ .

<sup>d</sup> Ref. [13].

Born–Oppenheimer vibronic states (e.g. between the ( $\nu=0$ )  $A^2\Pi$  and ( $\nu=0$ )  $B^2\Sigma^+$  states) are projected onto the states of interest (i.e. ( $\nu=0$ )  $A^2\Pi$  state or ( $\nu=0$ )  $B^2\Sigma^+$  state) by use of perturbation theory. The effective Hamiltonian operator for the  $X^2\Sigma^+$  ( $\nu=0$ ) and  $B^2\Sigma^+$  ( $\nu=0$ ) states included the rotation and its centrifugal distortion, the spin-rotation and the magnetic hyperfine interactions:

$$H^{\text{eff}}(2\Sigma) = T_v + BN^2 - DN^4 + \gamma \mathbf{N} \cdot \mathbf{S} + b_F \mathbf{I} \cdot \mathbf{S} + c \left( I_z S_z - \frac{1}{3} \mathbf{I} \cdot \mathbf{S} \right). \quad (5)$$

The effective Hamiltonian operator for the  $A^2\Pi$  ( $\nu=0$ ) state including the origin, spin-orbit interaction and associated centrifugal distortion correction, rotation and associated centrifugal distortion correction, and the  $\Lambda$ -doubling interaction terms:

$$H^{\text{eff}}(A^2\Pi) = T_v + AL_z S_z + A_D \frac{1}{2} [\mathbf{N}^2, L_z S_z]^+ + BN^2 - DN^4 + \frac{1}{2} (p+2q) (e^{2i\varphi} S_- J_- + e^{-2i\varphi} S_+ J_+) - \frac{1}{2} q (e^{2i\varphi} J_-^2 + e^{-2i\varphi} J_+^2). \quad (6)$$

In Eq. (6)  $J_{\pm}$  are the shift operators of the total angular momentum in the absence of the nuclear spin,  $[ ]^+$  is the anti-commutator, and  $\varphi$  is the azimuthal angle of the electron.

In the absence of an applied field levels are designated by the total angular momentum,  $F$ , and associated projection quantum number  $M_F$ . The field-free eigenvalues and eigenvectors for the  $X^2\Sigma^+$  and  $B^2\Sigma^+$  states were obtained by diagonalization of a  $4 \times 4$  matrix representation constructed using a Hund's case ( $a_{\text{H}}$ ), non-parity, basis set [6]. Although the proton magnetic hyperfine splitting was not resolved for the  $A^2\Pi$  ( $\nu=0$ ) state, the nuclear spin was included in the basis set to facilitate the prediction of the relative intensities (see below). Hence, for the  $A^2\Pi$  ( $\nu=0$ ) state an

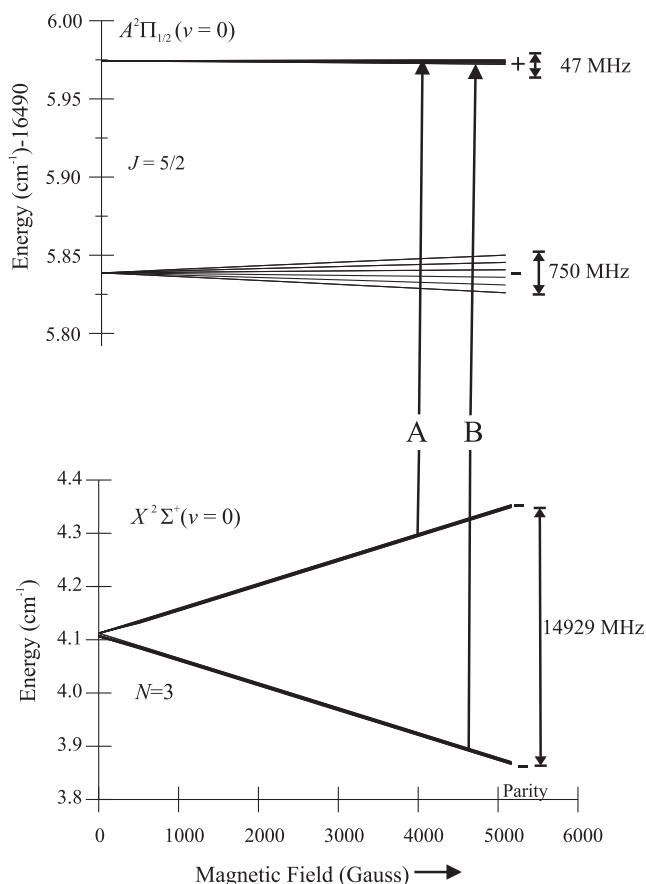


**Fig. 5.** The magnetic tuning of the levels associated with the  $P_1(3)$  and  $Q_{12}(3)$  lines of the (0,0)  $A^2\Pi_{1/2}-X^2\Sigma^+$  band. The numerical splittings indicated on the right hand side are from the lowermost to the uppermost level in each case, and are for a magnetic field of 5300 G.

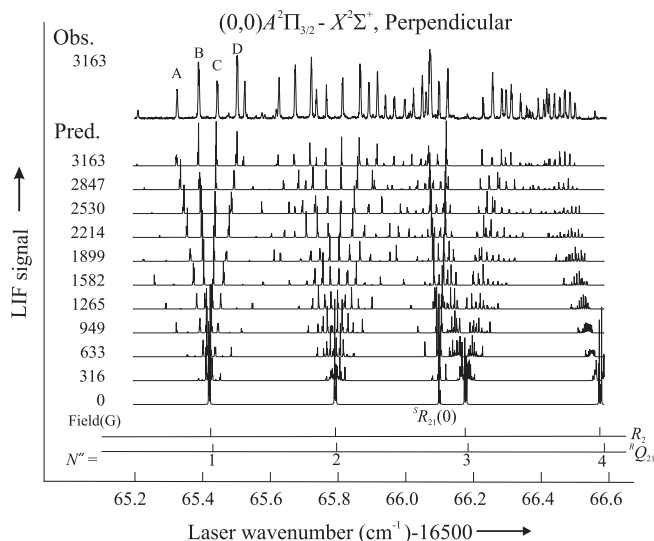


**Fig. 6.** The observed (top) and predicted (bottom) spectra in the region of the low- $J$   $R_{21}$  and  $R_2$  branch features of the (0,0)  $A^2\Pi_{3/2}-X^2\Sigma^+$  band recorded in the presence of a magnetic field oriented perpendicular ( $\Delta M_J = \pm 1$ ) to the electric field of the laser radiation. The energy levels associated with the “A–D” spectral features are given in Fig. 7.

$8 \times 8$  matrix representation was constructed and diagonalized to produce the eigenvalues and eigenvectors. A nonlinear least-squares fitting procedure program was written to optimize the parameters for the  $A^2\Pi$  ( $v=0$ ) and  $B^2\Sigma^+$  ( $v=0$ ) states. The rotational,  $B$  ( $=0.34248823 \text{ cm}^{-1}$ ), centrifugal distortion correction to rotation,  $D$  ( $=4.6899 \times 10^{-7} \text{ cm}^{-1}$ ), spin-rotational,  $\gamma$  ( $=0.0013138 \text{ cm}^{-1}$ ), Fermi contact,  $b_F$  ( $=0.0040895 \text{ cm}^{-1}$ ), and dipolar,  $c$  ( $=0.001111 \text{ cm}^{-1}$ ) parameters for the  $X^2\Sigma^+$  ( $v=0$ ) state were held fixed to those determined from the analysis of the millimeter wave spectrum [10]. The determined field-free spectroscopic parameters are presented in Table 3, where they are compared to a previous determination from the state-by-state analysis performed in Ref. [13]. A comparison with the parameters determined from the deperturbation analysis of Ref. [10] is not practical. With the exception of the centrifugal distortion correction to the spin-rotation parameter,  $A_D$ , the previously determined parameters are in good agreement with the more precisely determined values of the present study. The determined sign for  $A_D$  is consistent with that determined for CaH [14]. The difference in the presently determined values for  $A$  ( $=72.61743(47) \text{ cm}^{-1}$ ) and  $T_0$  ( $=16529.10177 \text{ cm}^{-1}$ ) as compared to those of Ref. [26] of  $72.589(2) \text{ cm}^{-1}$  and  $16529.134(1) \text{ cm}^{-1}$  is attributed to choice in effective Hamiltonian operator. Specifically, the  $\Lambda$ -doubling operator form used here produces a constant energy shift of  $p+2q$  ( $=-0.04481 \text{ cm}^{-1}$ ), causing the difference between  $A$  and  $T_0$  values.

The matrix representation of Zeeman operators given in Eq. (2) is block-diagonal in  $M_F$  but of infinite dimension. The expressions for the Hund's case ( $a_{\beta j}$ ) matrix element for the operators associated with the  $g_S$  and  $g_L$  terms can be found in Ref. [6] and those for the  $g_I$  term from Ref. [13]. The eigenvalues and eigenvectors of the ( $v=0$ )  $X^2\Sigma^+$  and ( $v=0$ )  $B^2\Sigma^+$  states were modeled by diagonalization of the  $24 \times 24$  matrix constructed using the Hund's case ( $a_{\beta j}$ ) basis set functions for the  $F \leq 5$  levels. Similarly, the eigenvalues and eigenvectors of the  $A^2\Pi$  ( $v=0$ ) state were modeled by diagonalization of a  $48 \times 48$  Hund's case ( $a_{\beta j}$ ) representation for the  $F \leq 5$  levels. This truncation was sufficient to reproduce the experimental accuracy ( $\pm 30 \text{ MHz}$ ) of the (0,0)  $B^2\Sigma^+-X^2\Sigma^+$  and (0,0)  $A^2\Pi-X^2\Sigma^+$  Zeeman data set, which includes maximum  $F$  values of 4.

The measured transition wavenumbers for the Zeeman spectra were used as input to a nonlinear least-squares fitting procedure program and the  $g$ -factors for the  $A^2\Pi$  ( $v=0$ ) and  $B^2\Sigma^+$  ( $v=0$ ) states optimized. The fine structure parameters were held fixed to those of Table 3. The  $g$ -factors for the  $X^2\Sigma^+$  ( $v=0$ ) state were held fixed to those expected for a free electron and predicted by Eq. (3):  $g_S = 2.002$  and  $g_I = -0.00194$ . These values are consistent with those determined from the matrix isolation study [8]:  $g_S = 2.0020$  and  $g_I = -0.002$ . The (0,0)  $B^2\Sigma^+-X^2\Sigma^+$  data were fit by optimizing both  $g_I$  and  $g_S$  for the  $B^2\Sigma^+$  ( $v=0$ ) state. Numerous fits of the (0,0)  $A^2\Pi-X^2\Sigma^+$  spectrum were attempted. The data set was insensitive to  $g_I$  values in the range expected (see below). In the end a satisfactory fit could be obtained by fixing  $g_S$ ,  $g_L$  and  $g_I$  to 2.002, 1.000 and 0.0, respectively and varying only  $g_I$ . The optimized  $g$ -factors and associated errors are presented in Table 4. The majority of lines in the Zeeman spectra are unresolved blends, which is responsible for the standard deviation of the fits of the (0,0)  $A^2\Pi-X^2\Sigma^+$  (0,0) ( $=0.00182 \text{ cm}^{-1}$ ) and  $B^2\Sigma^+-X^2\Sigma^+$  ( $=0.00136 \text{ cm}^{-1}$ ) bands being slightly larger than the field-free values of  $0.00103 \text{ cm}^{-1}$  and  $0.00081 \text{ cm}^{-1}$ .

The quantum number assignment of the Zeeman spectra was greatly assisted by modeling the spectra. A  $24 \times 24$  Hund's case ( $a_{\beta j}$ ) transition moment matrix for the (0,0) band of the  $B^2\Sigma^+-X^2\Sigma^+$  system or a  $24 \times 48$  Hund's case ( $a_{\beta j}$ ) transition moment matrix for the (0,0) band of the  $A^2\Pi-X^2\Sigma^+$  system was constructed. The transition moment was obtained by cross multiplication of the

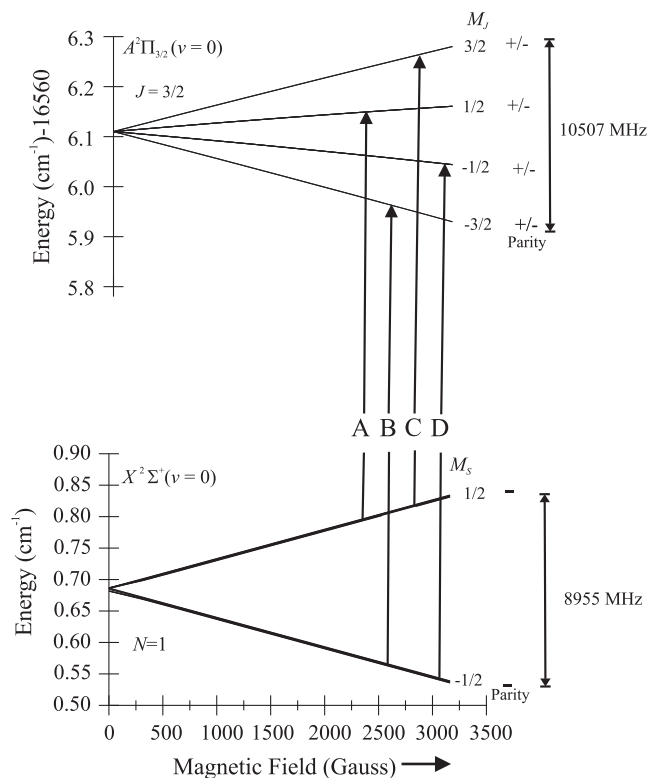


Fig. 7. The magnetic tuning of the levels associated with the  $R_{Q_{21}}$  and  $R_2$  lines of the (0,0)  $A^2\Pi_{3/2}-X^2\Sigma^+$  band and the associated assignment of the spectral features of Fig. 6. There is a slight non-linearity in tuning due to magnetic-field-induced interaction with the  $J=5/2$  levels. The numerical splittings indicated on the right hand side are for a magnetic field of 3163 G.

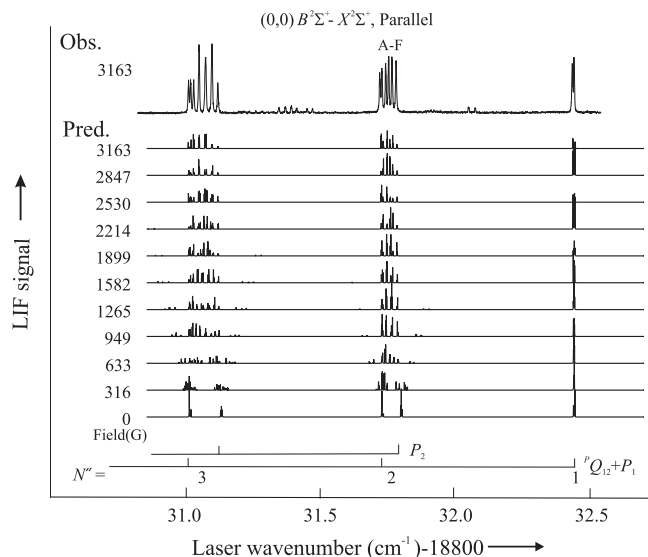
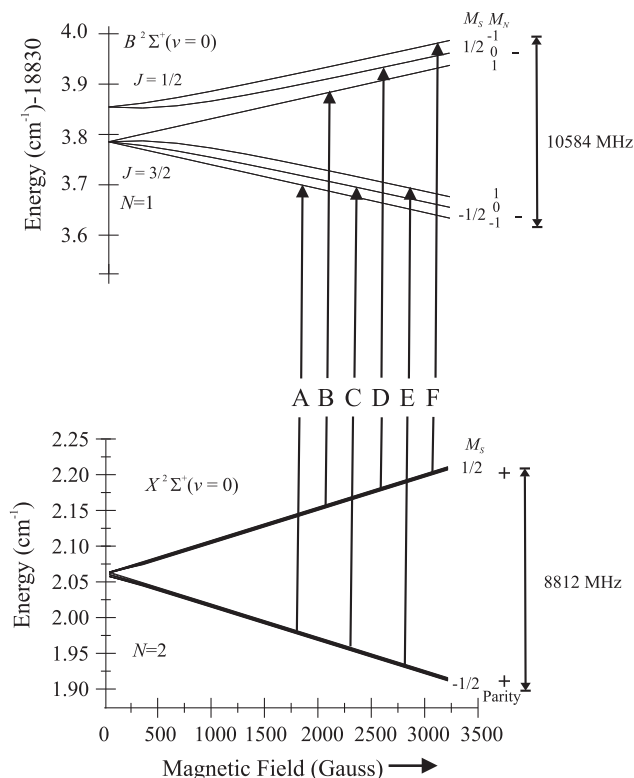


Fig. 8. The observed and predicted spectrum in the region of the low- $J$   $P_{Q_{12}}$ ,  $P_1$ , and  $P_2$  branch features of the (0,0)  $B^2\Sigma^+-X^2\Sigma^+$  band recorded in the presence of a 3163 G magnetic field oriented parallel ( $\Delta M_J = 0$ ) to the electric field of the laser radiation. The energy levels associated with the "A-F" spectral features are given in Fig. 9.

transition moment matrix by the Hund's case ( $a_{\beta j}$ ) eigenvectors. The transition moment was squared, multiplied by a Boltzmann factor commensurate with a rotational temperature of 10 K and used in conjunction with a Lorentzian linewidth of 30 MHz full width at half maximum to predict each spectral feature.



**Fig. 9.** The magnetic tuning of the energy levels associated with the  $^PQ_{12}(2)$  and  $P_1(2)$  lines of the  $(0,0)$   $B^2\Sigma^+-X^2\Sigma^+$  band. In the  $B^2\Sigma^+$  state  $M_J$  is the approximately good quantum number at low fields and  $M_S$  and  $M_N$  become approximately good quantum numbers at high field. The assignment of the “A–F” lines of Fig. 8 are indicated. The numerical splittings indicated on the right hand side are for a magnetic field of 3163 G.

**Table 4**  
The Zeeman parameters for the  $(v=0)$   $A^2\Pi$  and  $(v=0)$   $B^2\Sigma^+$  states of CaF.

$(v=0)$ $A^2\Pi$		$(v=0)$ $B^2\Sigma^+$	
Parameter	Fit <sup>a</sup>	Parameter	Fit <sup>b</sup>
$g'_L$	1.000	$g_L$	0.0696 (82)
$g'_I$	−0.0611 (37)	$g_S$	1.9977 (53)
$g_S$	2.0023		
Std. dev. of fit ( $\text{cm}^{-1}$ )	0.00182 (0.00183) <sup>b</sup>		0.00136 (0.00137) <sup>b</sup>

<sup>a</sup> Obtained from fitting the transitions wavenumbers of the  $(0,0)$   $A^2\Pi-X^2\Sigma^+$  and  $(0,0)$   $B^2\Sigma^+-X^2\Sigma^+$  bands with the  $g$ -factors for the  $X^2\Sigma^+$  fixed at  $g_S = 2.002$  and  $g_I = -0.00194$ . The numbers in parentheses represent a  $2\sigma$  statistical error estimate. All values without error limits were held fixed.

<sup>b</sup> The numbers in parentheses are the values obtained when  $g'_I$  ( $v=0$ )  $A^2\Pi$  and  $g_L$  ( $v=0$ )  $B^2\Sigma^+$  are constrained to the values predicted by the “Curl-type relationship of −0.0642 and 0.0674, respectively, and  $g_S$  ( $v=0$ )  $B^2\Sigma^+$  is constrained to 2.0023.

## 5. Discussion

The precisely determined fine structure parameters for the  $(v=0)$   $A^2\Pi_r$  and  $(v=0)$   $B^2\Sigma^+$  states given in Table 3 will be useful for predictions of the optical transitions associated with the planned laser cooling experiments. The very small standard deviation of the field-free fits of  $0.00103 \text{ cm}^{-1}$  and  $0.00081 \text{ cm}^{-1}$  for the  $(0,0)$   $A^2\Pi-X^2\Sigma^+$  and  $(0,0)$   $B^2\Sigma^+-X^2\Sigma^+$  bands, respectively, illustrates that the individual state analysis using the effective Hamiltonian approach is both convenient and efficient for reproducing the energies of the low-rotational levels.

The magnetic tuning of the low rotational levels in the  $(v=0)$   $A^2\Pi_{1/2}$ ,  $(v=0)$   $A^2\Pi_{3/2}$ , and  $(v=0)$   $B^2\Sigma^+$  electronic states, which will

be used in the proposed MOT, have been precisely determined using the effective Hamiltonian approach. It turns out that the tuning is very accurately predicted by assuming that  $g'_L = 1.000$  and  $g_S = 2.002$  and using Eqs. (3) and (4) to predict  $g_L$  and  $g'_I$ . These relationships predict that  $g_L$  ( $B^2\Sigma^+$ ) = +0.0672 and  $g'_I$  ( $A^2\Pi_r$ ) = −0.0653. It is more difficult to estimate  $g_L$  ( $A^2\Pi_r$ ) from the Curl relationship because the required spin-rotation parameter,  $\gamma$ , for the  $(v=0)$   $A^2\Pi$  state is not determined. Brown and Watson [17] have shown that  $\gamma$  and  $A_D$  are totally correlated for a  $^2\Pi$  state and that when  $\gamma$  is constrained to zero, as was done in the field free analysis performed here, then [17]:

$$A_D^{\text{Fitting}} \approx A_D^{\text{True}} - \gamma \frac{2B}{(A-2B)}. \quad (7)$$

Assuming that  $A_D^{\text{True}} = 0$ , then the upper limit for  $\gamma$  ( $(v=0)$   $A^2\Pi$ ) is  $0.0154 \text{ cm}^{-1}$ , which gives an upper limit for the predicted  $g_L$  ( $(v=0)$   $A^2\Pi$ ) of −0.022. As mentioned above the data set is particularly insensitive to  $g_L$  ( $(v=0)$   $A^2\Pi$ ) values of this magnitude and it was constrained to zero. Using these predicted values for the  $g$ -factors, along with  $g_S$  and  $g'_L$  of 2.002 and 1.000, resulted in standard deviation of  $0.00183 \text{ cm}^{-1}$  and  $0.00137 \text{ cm}^{-1}$  for the  $(0,0)$   $A^2\Pi-X^2\Sigma^+$  and  $(0,0)$   $B^2\Sigma^+-X^2\Sigma^+$  bands, respectively, which are only slightly larger than the values of  $0.00182 \text{ cm}^{-1}$  and  $0.00132 \text{ cm}^{-1}$  obtained using the optimized set of parameters. Although the success of the Curl relationship predictions for the  $(0,0)$   $A^2\Pi-X^2\Sigma^+$  band might have been expected because the  $(v=0)$   $A^2\Pi$  state is isolated, the agreement for the  $(0,0)$   $B^2\Sigma^+-X^2\Sigma^+$  band is a bit surprising given that the energies of the  $(v=0)$   $B^2\Sigma^+$  state are nearly degenerate with the  $(v=4)$   $A^2\Pi$  levels. Evidently the vibrational overlap integral is diminishingly small. A similar combination of the effective Hamiltonian approach and use of the Curl relationships is expected to accurately predict the magnetic tuning of the low-rotational branch features of the  $(0,0)$   $A^2\Pi-X^2\Sigma^+$  and  $(0,0)$   $B^2\Sigma^+-X^2\Sigma^+$  bands of SrF, even though the  $B^2\Sigma^+ \leftrightarrow A^2\Pi$  interaction is much larger than that in CaF. The prediction of the Zeeman tuning of lines in the  $(0,0)$   $A^2\Pi-X^2\Sigma^+$  and  $(0,0)$   $B^2\Sigma^+-X^2\Sigma^+$  bands involving higher rotational lines than those used in the current analysis (i.e.  $J > 7/2$ ) will be more subject to errors associated with local perturbations and the effect of the rotational induced magnetic moment.

## Acknowledgments

This research has been supported by the National Science Foundation, Division of Chemistry, CHE-1265885 (ASU), and, in the UK, by the EPSRC under Grant EP/I012044/1.

## Appendix A. Supplementary material

Supplementary data for this article are available on ScienceDirect ([www.sciencedirect.com](http://www.sciencedirect.com)) and as part of the Ohio State University Molecular Spectroscopy Archives ([http://library.osu.edu/sites/msa/jmsa\\_hp.htm](http://library.osu.edu/sites/msa/jmsa_hp.htm)). Supplementary data associated with this article can be found, in the online version, at <http://dx.doi.org/10.1016/j.jms.2015.07.009>.

## References

- [1] J.F. Barry, D.J. McCarron, E.B. Norrgard, M.H. Steinecker, D. DeMille, Nature 512 (2014) 286.
- [2] D.J. McCarron, E.B. Norrgard, M.H. Steinecker, D. DeMille, New J. Phys. 17 (2015) 035014.
- [3] V. Zhelyazkova, A. Cournol, T.E. Wall, A. Matsushima, J.J. Hudson, E.A. Hinds, M.R. Tarbutt, B.E. Sauer, Phys. Rev. A 89 (2014) 053416.
- [4] M.R. Tarbutt, New J. Phys. 17 (2015) 015007.
- [5] E.L. Hill, Phys. Rev. 34 (1929) 1507.
- [6] W. Watson, Phys. Rev. 39 (1932) 278.



- [7] J.M. Brown, A. Carrington, *Rotational Spectroscopy of Diatomic Molecules*, Cambridge University Press, Cambridge, 2003.
- [8] W. Weltner Jr., *Magnetic Atoms and Molecules*, Dover Publications Inc., New York, 1983.
- [9] R.F. Curl, *Mol. Phys.* 9 (1965) 585.
- [10] M.A. Anderson, M.D. Allen, L.M. Ziurys, *Astrophys. J.* 424 (1994) 503.
- [11] L.A. Kaledin, J.C. Bloch, M.C. McCarthy, R.W. Field, *J. Mol. Spectrosc.* 197 (1999) 289–296.
- [12] M. Dulick, P.F. Bernath, R.W. Field, *Can. J. Phys.* 58 (1980) 703–712.
- [13] J. Vergès, C. Effantin, A. Bernard, A. Topouzkhianian, A.R. Allouche, J. d'Incan, R.F. Barrow, *J. Phys. B* 26 (1993) 279–284.
- [14] J. Chen, J. Gengler, T.C. Steimle, J.M. Brown, *Phys. Rev. A* 73 (2006) 012502.
- [15] E.J. Salumbides, K.S.E. Eikema, W. Ubachs, U. Hollenstein, H. Knoeckel, E. Tiemann, *E. Phys. J.D: At. Mol. Opt. Plasma Phys.* 47 (2) (2008) 171.
- [16] N. Beverini, E. Maccioni, F. Strumia, *J. Opt. Soc. Am. B* 15 (1998) 2206–2209.
- [17] J.M. Brown, J.K.G. Watson, *J. Mol. Spectrosc.* 65 (1977) 65.